Energy dependence of $p + {}^{232}$Th fission mass distributions: Mass-asymmetric standard I and standard II modes, and multichance fission

A. C. Berriman,[1] D. J. Hinde,[1,*] D. Y. Jeung,[1] M. Dasgupta,[1] H. Haba,[2] T. Tanaka,[1] K. Banerjee,[1,†] T. Banerjee,[1,‡] L. T. Bezzina,[1] J. Buete,[1] K. J. Cook,[1,3] S. Parker-Steele,[1,§] C. Sengupta,[1,‖] C. Simenel,[1,4] E. C. Simpson,[1] M. A. Stoyer,[1,5] B. M. A. Swinton-Bland,[1] and E. Williams[1]

[1]*Department of Nuclear Physics and Accelerator Applications, Research School of Physics, The Australian National University, Canberra, ACT 2601, Australia*

[2]*Nishina Center for Accelerator-Based Science, RIKEN, Wako, Saitama 351-0198, Japan*

[3]*Facility for Rare Isotope Beams, Michigan State University, 640 South Shaw Lane, East Lansing, Michigan 48824, USA*

[4]*Department of Theoretical Physics, Research School of Physics, Australian National University, Canberra, ACT 2601, Australia*

[5]*Nuclear and Chemical Sciences Division, Lawrence Livermore National Laboratory, Livermore, California 94550, USA*

(Received 3 May 2022; accepted 3 June 2022; published 23 June 2022)

Background: The predominant mass-asymmetric fission of actinide nuclides occurs mainly through the so-called standard I and standard II modes. Though understood to be caused by shape-dependent shell structures encountered between the fission barrier deformation and scission, the most relevant shell gaps are still not firmly established. The standard I mode had been associated with the spherical doubly magic ^{132}Sn, and thus the $Z = 50$ proton shell, but recently it has been proposed that standard I and standard II are associated with quadrupole and octupole deformed gaps at $Z = 52$ and 56, respectively.

Purpose: We investigate how the relative probabilities of the standard I and standard II modes vary with excitation energy near threshold, probing where the two modes bifurcate.

Methods: The Australian National University Heavy Ion Accelerator Facility and CUBE fission spectrometer have been used to measure fission mass distributions for the $p +^{232}$ Th reaction (forming ^{233}Pa) at closely spaced bombarding energy intervals from 6.5 to 28 MeV.

Results: A model-independent analysis of the energy dependence of the shape of the mass-asymmetric peak shows a strong dependence of the standard I and standard II relative probability on excitation energy near threshold.

Conclusions: The results are consistent with the standard II mode having a lower fission barrier than standard I in ^{233}Pa, with the latter increasing continually in relative probability above its barrier energy. It is concluded that multichance fission, in particular last chance fission, plays a strong role in determining the observed energy dependence of all fission modes.

DOI: 10.1103/PhysRevC.105.064614

I. INTRODUCTION

The discovery of nuclear fission [1] came through the identification [2] of the element Ba (atomic number $Z = 56$), produced following the irradiation of uranium ($Z = 92$) by neutrons. This corresponds to a significantly asymmetric charge division in the fission of uranium. It is now known [3] that predominantly asymmetric division of mass and charge is almost universal in spontaneous and low energy fission of isotopes of actinide elements. The concept of observed fission mass distributions at low excitation energies, E_x, being a superposition of different distributions, with different fission barriers, was introduced by Turkevich and Niday [4]. At E_x above 40 MeV, measured mass distributions become peaked at mass symmetry [5]. However, because fission may also occur after emission of one or more neutrons [4,6] (known as *multichance fission*), even at high initial E_x, mass-asymmetric fission from low E_x still contributes [6,7].

The liquid drop model predicts that the lowest barrier between the ground state and a scission configuration corresponds to a symmetric mass split. The prevalence of mass-asymmetric fission is attributed to shape-dependent modulation of the liquid drop potential energy surface due to shell gaps in the single particle levels [3]. These may result in lower fission barriers for asymmetric mass and charge division, and furthermore to valleys in the potential energy surface leading to scission.

*Corresponding author: david.hinde@anu.edu.au

†Present address: Variable Energy Cyclotron Centre, 1/AF, Bidhan Nagar, Kolkata 700064, India.

‡Present address: Istituto Nazionale di Fisica Nucleare, Sezione di Napoli, 80126 Napoli, Italy.

§Present address: Ark King Solomon Academy, Penfold Street, London NW16RX, England, United Kingdom.

‖Present address: ACRF Image X Institute, University of Sydney, Sydney, Australia.

A. Fission modes

Fissions with different distributions of observable characteristics [fragment mass, total fragment kinetic energy (TKE)] are commonly called "modes." They have been associated with the presence of valleys in the multidimensional potential energy surface. The valleys may be separated from each other by significant potential barriers [8], which can result in little or no coupling between the modes after the division of flux to different valleys. The principal modes in actinide fission, named by Brosa *et al.* [9], are the mass-symmetric "superlong" mode (SL), generally associated with the liquid drop mass-symmetric fission barrier, and two mass-asymmetric modes. The mass-asymmetric mode closest to mass symmetry is the "standard I" mode (StI), having the highest fission fragment total kinetic energy [10,11]. This is associated with a compact shape at scission. Slightly further from mass symmetry is the "standard II" mode (StII), with somewhat lower TKE corresponding to a more elongated scission shape. Moving further from symmetry, less probable modes postulated from theoretical expectations and/or fits to experimental data include the "standard III" mode and superasymmetric modes [9,12–15].

The underlying shell structure resulting in the dominant mass-asymmetric StI and StII modes is still debated [3,16]. Because the mean mass of the heavy fragment is observed to be approximately independent of the mass of the fissioning nucleus across the actinide region [17], shell effects in the nascent *heavy* fragment are understood to play the dominant role. The StI mode has long been associated with the spherical doubly magic ^{132}Sn nucleus [3,18]. Although the StI heavy fragment mass is slightly greater than 132, nucleons from the neck between the two nascent fragments have been postulated to account for the additional mass. The StII mode was once thought to be associated with neutron number $N = 88$, corresponding to a quadrupole deformed shape of the heavy fragment. However, systematic measurements using relativistic fragmentation reactions giving integer charge identification of the final fission fragments [19] showed that both the StI and StII modes are strongly correlated with proton numbers in the heavy fragments, rather than neutron numbers, these averaging $Z = 52.5$ and 55, respectively, for StI and StII.

Recently, it was suggested [16] that these dominant mass-asymmetric fission modes may both be associated with octupole-deformed proton shell gaps at $Z = 52$ and 56. The neck between two fragments close to scission can be mapped to two octupole deformed fragments in contact [16], so in principle the introduction of octupole deformation of the nascent fragments can explicitly account for the nucleons making up the neck expected to exist between the fragments at scission. Depending on the deformations, the shell gaps playing the major role at the fission saddle-point deformation could be different from those defining the (observed) fragments produced at scission.

To probe experimentally the full fission path from ground-state deformation to scission seems impossible. However, a key question in the dynamics can be addressed, that is, where the StI and StII modes bifurcate, i.e., at what deformation does the fissioning system "decide" to undergo scission corresponding to the StI or StII modes? Information on this question can be inferred from experimental observables that are sensitive to the bifurcation point.

In this paper, the dependence of the relative probability of the StI and StII modes on excitation energy is investigated. If the bifurcation point is after the fission barrier has been crossed, the relative probability of the two fission modes would not be expected to have a rapid dependence on excitation energy. On the other hand, if the StI and StII modes had different excitation energy thresholds (different fission barrier heights), at near-threshold excitation energies a rapid dependence of relative probability on excitation energy would be expected.

B. Separating shell effects and proton pairing effects

Recent experimental results [19,20] have confirmed another source of structure in fission mass distributions. It was proposed in the 1970s [17] that fine structure observed in spontaneous fission mass distributions is correlated with even-Z fragment pairs. Because final fragment masses rather than charges were measured, neutron evaporation from the fragments limited the mass resolution of the experiments. Thus structures associated with pairing showed relatively small amplitude. In recent years this suggestion has been spectacularly confirmed, with ever-increasing clarity, using relativistic fragmentation reactions to produce many actinide nuclides having high velocity in the laboratory frame [19,20]. This permits the Z of both fragments to be uniquely identified experimentally, allowing Coulomb-induced fission from interactions with a secondary target to be isolated, and Z distributions determined with high accuracy. The staggering in yield between fragment pairs both having even Z and odd Z can be very large at low excitation energy, also seen clearly in fragment Z distributions determined by decay counting [21].

This is a great achievement, but raises a significant issue in interpretation of fission mass or Z distributions: can these proton pairing effects be disentangled from shell effects? The period of pairing structure is two units in Z, so approximately 5 u in mass. The separation between shell gaps in heavy nuclei with spherical shapes is very large. However, as more shape degrees of freedom are considered, spacing in mass between shell gaps reduces dramatically. A good example comes from the StI and StII mass-asymmetric fission modes. Empirical systematics showed the modes differ only by $Z = 2.5$. They were subsequently proposed to be associated with deformed quadrupole and octupole shapes of the heavy fragment with $Z = 52$ and 56. Thus both experimentally and theoretically, the separation in mass and charge of important shell gaps can be close to that from pairing.

The effects of proton pairing can be minimized by studying the fission of odd-Z nuclei. Given the very small proton emission probability in low energy fission, essentially all pairs of fission fragments comprise one with even Z, and one with odd Z. Much smoother fission Z distributions from odd-Z nuclei are seen [20] in relativistic radioactive beam measurements of fission of Ac ($Z = 89$) and Pa ($Z = 91$). Indeed within

experimental uncertainties no evidence is seen for proton odd-even staggering [20].

In conclusion, to isolate structure in fission mass distributions due to shells, the simplest approach is to study fission mass distributions of odd-Z nuclei, where any structures seen should essentially result from shell effects.

C. Goal of the current paper

In this paper the goal is to investigate whether the mass-asymmetric standard I and standard II fission modes have different energy thresholds (fission barriers) by measuring mass distributions for fission of the odd-Z nucleus $^{233}_{91}$Pa, formed in $p + ^{232}$Th reactions. A considerable number of measurements have been made for this reaction in the past, as will be discussed in detail later. Our measurements differ in the low beam energies and small beam energy steps used. This allows investigation of the detailed dependence on beam energy of scission mass distributions, and thus the dependence on excitation energy.

II. EXPERIMENTAL DETAILS

Beams of protons were provided by the 14UD tandem electrostatic accelerator of the Australian National University Heavy Ion Accelerator Facility. In two separate experiments, terminal voltages between 3.25 and 14 MV were employed to deliver beams from 6.5 to 28 MeV, with beam currents up to 500 nA. A dc beam, which allowed the largest beam currents, was used in 2/3 of the measurements, taken in the first experiment. Pulsed beams were used in the second experiment, with 700-ps full width at half maximum, and pulse separation 106.7 ns. This allowed determination of individual fragment velocities as described in Sec. III.

The target of ^{232}Th was vacuum deposited onto an Al backing of $\approx$60 μg/cm^2, having ^{232}Th areal density $\approx$65 μg/cm^2. The target normal was oriented at 45° (dc beam measurements) or 60° (pulsed beam measurements) to the beam axis. A voltage of +13 to +15 kV was applied to the target to suppress electrons. Its effect on the beam energy was accounted for. The target backing faced downstream and, together with the chosen target orientations, minimized the effects of energy loss of fission fragments in the target.

Fission fragments were detected using the CUBE spectrometer [22–24], consisting of two (dc measurements) or three (pulsed beam measurements) large area position sensitive multiwire proportional counters (MWPCs) with active area up to 279×357 mm. The detectors were placed with their normals 180 or 195 mm from the target. The geometries for the measurements are shown in Figs. 1(a) and 1(b).

The accuracy of the experimental techniques and a new time difference analysis method for dc beam measurements [25] was checked in a benchmarking measurement of the spontaneous fission mass distribution for ^{248}Cm. The source consisted of 25 μg/cm^2 of ^{248}Cm, deposited as the nitrate over a 3×5 mm area on an Al foil, determined by energy loss measurement to be 205 μg/cm^2 in thickness. Consistent Cm thickness values were obtained from decay counting and ^{58}Ni sub-barrier elastic scattering yields and energies, measured in ion-implanted Si monitor detectors located at 22.5° scattering angle.

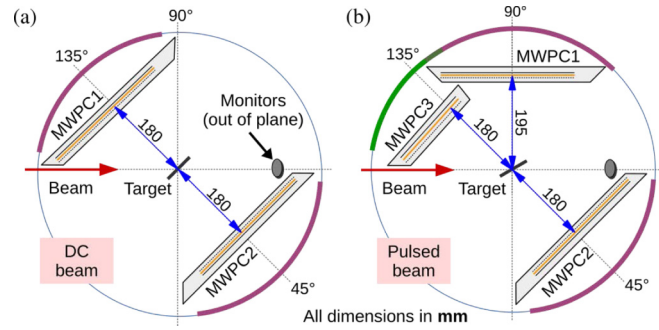

FIG. 1. Experimental configurations used for (a) dc beam measurements and (b) pulsed beam measurements.

III. DATA ANALYSIS

The goal of the analysis is to determine fission fragment mass spectra from the timing and position information provided by the MWPC detectors. Deriving them from the raw data requires a different approach depending on whether a dc or pulsed beam was used. For a dc beam, a new time difference method was applied, whereas the double velocity ($2v$) method was used with pulsed beams. Both methods are described below. They provide fission mass ratios $M_R = M_{F1}/(M_{F1} + M_{F2})$ where M_{F1} and M_{F2} are the fragment masses at *scission*. In contrast, the double energy ($2E$) method [11,17] provides the mass ratio of the fission fragments that enter the detectors. These masses are smaller than those at scission because of deexcitation of the fragments by particle (mainly neutron) evaporation after scission.

It is convenient to present experimental data in terms of the fragment masses at scission, since this is what theoretical models of fission dynamics directly calculate. Both the double velocity and time difference methods are based on conservation of momentum, so the mass of the fissioning nucleus has to be *assumed* to obtain the fragment masses. For actinide targets the fission cross sections are very much larger than from any lighter impurity element in the target. Thus as long as the desired actinide nuclide is predominant in the target, the mass of the compound nucleus can be obtained. Prescission neutron emission could be assumed to be zero, as it is in this work, where low excitation energies result in small multiplicities. Alternatively the average effect can be corrected for according to measurements or systematics [5].

The mass spectra at scission presented in this paper define the fragment mass number A at scission in terms of the compound nucleus mass $A_{\rm CN}$ and the experimentally determined M_R through $A = M_R\, A_{\rm CN}$.

In the analysis of both the dc beam and pulsed beam measurements, energy loss corrections were applied iteratively, event by event, to the energy of the beam particles and the detected fission fragments. It was assumed that the reaction occurred at the center of the Th layer. The conclusions from the present paper rest on rather small differences in the shapes of the mass distributions from one beam energy to the next.

Thus it is important to demonstrate that the experimental and analysis methods do not introduce spurious features in the mass spectra. Thus the details of the two analysis methods specific to these proton-induced fission measurements are given below. A comprehensive comparison of the results from dc and pulsed beam measurements is made in Appendix B, which also describes the sensitivity of the results to calculations of the fragment energy losses in the target.

A. Time difference method

The determination of fission mass split from the measured time difference between the detection of the two fission fragments was first described in Ref. [26]. For fission events where no neutrons were emitted from the fragments (very high TKE events), unit fragment mass resolution was achieved.

An approach to make the time difference method generally applicable to fission from systems that do emit neutrons, and have small or zero center-of-mass velocity, was presented by Swinton-Bland *et al.* [25]. This method requires an *external* input: the center-of-mass relative velocities K of the two fission fragments as a function of mass split or fragment mass. This information can come from previous direct measurement of TKE, or from expectations from systematics—such as the Viola systematic average TKE values [27] extended to mass-asymmetric splits [28,29]. In the absence of structure in the TKE resulting from shell effects, it can be shown that to a good approximation K is independent of mass split.

The method was first applied to measurements of near-threshold fission of Bi isotopes [25], where the fission cross sections are typically small, and thus any systematic errors associated with using TKE values based on Viola systematics should be far outweighed by statistical uncertainties. However, a comparison was also shown in Ref. [25] of relatively high statistics mass distributions, analyzed using the time difference method, with previously published data from double energy measurements [30,31]. For the relatively narrow fission mass distributions seen in the $p + {}^{204}$Pb reaction, the two methods showed satisfactory agreement.

A high statistics ^{248}Cm spontaneous fission mass distribution determined using the double energy method (corrected for neutron emission from the fragments) is compared in Appendix A with the present time difference measurement analyzed using the approach described in Ref. [25]. The two distributions are in excellent agreement, supporting the application of this analysis to the wide fission mass distributions following the $p + {}^{232}$ Th reaction.

Mass distributions (from the same raw experimental data set) are presented in Appendix B, extracted using different mean TKE inputs to the time difference method. These are compared with the most accurate mass distribution, determined using the beam pulsing information that provides experimental fragment velocities event by event. Where the time difference method makes use of information on the mean TKE as a function of mass split for the specific fissioning nucleus [which could come from experiment, or from calculations, for example using the general description of the fission process (GEF) code [32]], the results are almost indistinguishable from the event-by-event double velocity analysis. In fact, uncertainties arising from fragment energy loss in the target can result in larger uncertainties in the mass spectra, as detailed in Appendix B.

All the results from dc beam measurements shown subsequently in this paper make use of the optimal time difference analysis method. This uses mean fragment relative velocities as a function of mass split derived from the experimental TKE data presented by Mulgin *et al.* [11]. Results were there presented for a number of proton energies, showing a smooth evolution with beam energy. For our measurements at intermediate energies, the dependence of K on mass split was interpolated.

Repeat measurements at a given energy using dc and pulsed beams, and analysis of pulsed beam data by both the $2v$ and time difference methods, show negligible difference in the characteristics of the mass spectra that are investigated in this paper. This gives confidence that the experimental mass distributions are not compromised by the reduced experimental information from dc beam time difference measurements. The results presented here are thus expected to be accurate.

B. Double velocity method

Data analysis of the pulsed beam measurements used a modification of the kinematic coincidence method that has been applied extensively in the analysis of experimental data taken previously with the CUBE spectrometer [22,23]. This analysis method makes use of the rf reference signal from the accelerator pulsing system, the time of which is recorded with each pair of fission fragments (detected within 100 ns of each other). The time difference T_0 between the rf signal and the passage of the beam pulse through the target must be determined, which is different for each beam energy.

In near-barrier heavy ion reactions, T_0 has been obtained by requiring the mean deduced fission source velocity to be equal to the calculated compound nucleus velocity (normally the center-of-mass velocity) [22]. In the case of proton beams, the center-of-mass velocity $v_{\mathrm{c.m.}}$ is only $\approx$2% of the fragment velocities. This means that $<$1 mm deviations in beam spot position on the target, combined with slight nonplanarity of the target, as well as the intrinsic angular spread of the fission fragments due to neutron evaporation, make it impossible to accurately determine T_0 in this way.

To overcome this issue, in this paper the value of T_0 for each beam energy was determined by matching TKE with expectations. It can be easily shown that TKE is much more sensitive to T_0 than masses (as demonstrated above through the extraction of masses without absolute time information). To reduce ambiguity, the TKE at mass symmetry was chosen to be matched with that determined by direct measurement of the fragment kinetic energies (using Si detectors) reported by Mulgin *et al.* [11]. A small correction ($\approx +2\%$) to the TKE values of Mulgin *et al.* was applied to account for neutron emission [33] from the fragments. Because the mass distributions are not very sensitive to the TKE (see Appendix B), at all proton energies the mass-symmetric TKE was set to the corrected value corresponding to the measurement for $E_p = 10.3$ MeV, namely, TKE $= 160.3$ MeV.

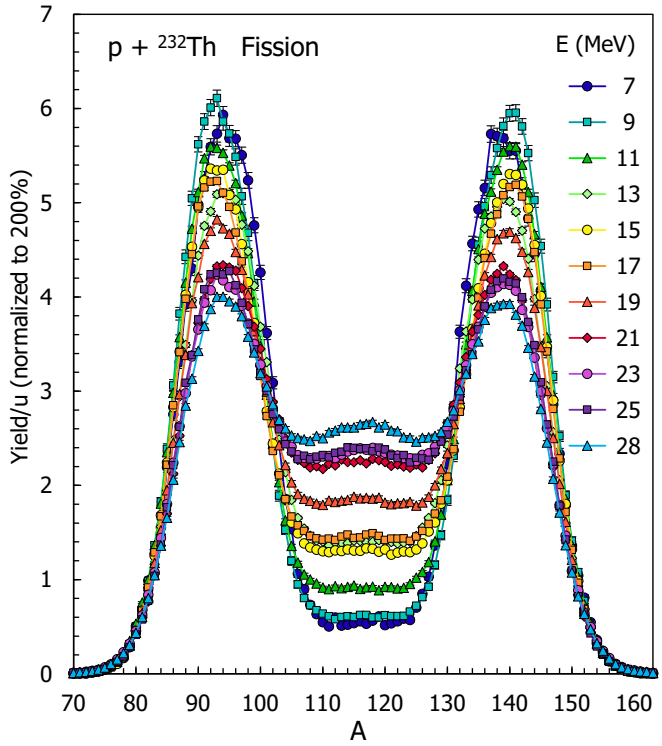

FIG. 2. Spectra of fission yield per mass unit (normalized to 200%) at the indicated nominal beam energies. The precise energies taking into account target ladder bias and energy losses are given in Table I. The yield at mass symmetry shows an irregular increase with beam energy associated with multichance fission. The position of the mass-asymmetric peak shows a small periodic shift with beam energy as shown in Fig. 5 and discussed in the text.

TABLE I. Nominal beam energy E, beam energy in the center of the Th target layer E_p, pulsed (ac) or dc beam, and excitation energy E_x assuming no preequilibrium emission.

E	E_p (MeV)	ac	dc	E_x (MeV)
6.5	6.450		✓	11.669
7	6.980		✓	12.196
8	7.971	✓		13.184
9	8.987		✓	14.195
10	9.984	✓		15.188
11	10.983		✓	16.182
11	10.984	✓		16.184
13	12.983		✓	18.174
14	13.985		✓	19.171
15	14.997		✓	20.179
17	16.990	✓		22.163
19	18.988		✓	24.153
21	20.990		✓	26.146
23	22.977		✓	28.125
25	24.982		✓	30.121
25	24.992	✓		30.131
28	27.997		✓	33.124

IV. EXPERIMENTAL RESULTS AND INTERPRETATION

To quantify the changes in the experimental fission mass distributions with beam energy, three approaches have been used. First the mass spectra were fitted by Gaussian functions representing the different fission modes. Second, a simple model-independent analysis of the shape of the mass-asymmetric peak was been carried out, providing significant insights. Finally the model-independent experimental characteristics were compared with the same quantities evaluated from calculations using the GEF code (version 2018/1.1), which reproduces systematic trends in fission characteristics over the actinide region and beyond.

A. Mass spectra as a function of beam energy

Mass spectra for fission of ^{233}Pa following $p + ^{232}$Th reactions are shown in Fig. 2. The nominal proton beam energies are indicated, and exact energies are given in Table I. Additional measurements at intermediate energies are not shown here. Their characteristics are intermediate between the distributions shown, and salient features are presented in subsequent figures. The spectra have not been mirrored, and because of small calibration uncertainties the light fragment peak yields are slightly higher than those of the heavy fragment peaks. Avoiding mirroring gives two independent measurements of the asymmetric peak characteristics. As is common in presentation of fission mass spectra, yields per mass unit have been normalized to 200% (two fission fragments per fission event). Thus the increase with energy (as expected) of the mass-symmetric component naturally reduces the height of the mass-asymmetric peaks.

The well-known increase in the fraction of mass-symmetric fission with increasing energy is clearly seen. However, it is also clear that this increase is not monotonic. Certain energy ranges show little change (7–9, 13–17, and 21–25 MeV), whereas there are rapid changes centered on 11 and 19 MeV. Presented in Sec. IV F in terms of excitation energies introduced in the proton reactions, this is clearly related to multiple chance fission. Because of the normalized mass spectra, the irregular behavior must result in irregular changes in the mass-asymmetric peak heights.

B. Fitting the mass spectra

The total yield in the *mass-asymmetric* peak clearly depends on the probability of the mass-symmetric mode, as noted above. The energy dependence of the *shape* of the mass-asymmetric peak itself will depend on the relative probabilities of the constituent mass-asymmetric fission modes, their individual dependence on excitation energy, and the distribution of fission chances (excitation energies) at a given proton beam energy. Thus potentially quite complex behaviors could result.

Close inspection of the experimental data in Fig. 2 near the maxima of the asymmetric peaks shows a change with beam energy of the mass at the maximum in yield. This is clearly seen by comparing the 7- and 9-MeV peaks, and the 13- and 17-MeV peaks. Since the StI and StII modes are centered at different masses, it is natural to relate this behavior to the energy dependence of the relative

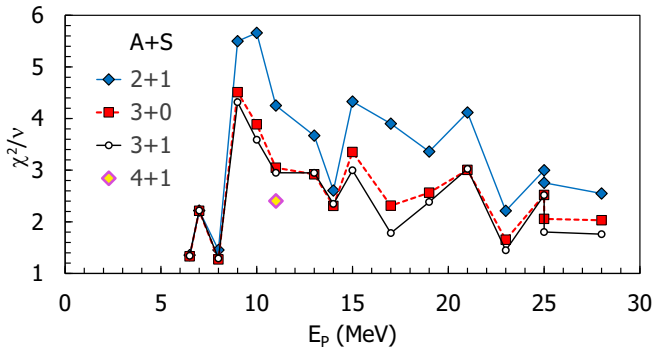

FIG. 3. The fit quality represented by chi squared per degree of freedom (χ^2/ν) for various parametrizations of the mass spectra, as a function of proton beam energy E_p. The legend shows the number of mass-asymmetric (A) and mass-symmetric (S) modes included in the fits, as for example $3+1$. Smaller χ^2/ν values at low E_p result from lower experimental statistics.

probabilities of these mass-asymmetric modes. To investigate these probabilities, it has been common to decompose the fission mass spectrum into a symmetric and several mass-asymmetric Gaussians, representing the mass-symmetric superlong and standard mass-asymmetric fission modes.

Information from the TKE is valuable to decompose the different modes [10–12]. In this paper the interpretation focuses on information from the mass spectra alone. In fact, by taking a novel approach that involves no mode decomposition, important information can be gleaned, as described in Sec. IV C. Analysis of mass-energy distributions for fission following proton interactions with a range of actinide nuclei will be the subject of a subsequent paper.

The mass spectra were fitted with a number of mass-asymmetric Gaussians and a mass-symmetric Gaussian. The mass-asymmetric pairs of Gaussians were mirrored about mass symmetry. Their common characteristics (mass offsets from symmetry, widths, and areas) were unconstrained in the fits. Only the position of the mass-symmetric Gaussian was fixed, at mass symmetry.

It was found that the aim of extracting the energy dependence of the StI and StII mode yields from fitting the full mass distributions is hostage to assumptions about the form and number of the fission modes contributing to the full mass spectrum. If the centroids and widths of the modes were defined, such issues would be reduced. However, because of multichance fission, defining their energy dependence would itself involve many assumptions.

Details of several Gaussian fitting scenarios are provided below, from which the above conclusions were obtained.

1. Five Gaussian fitting

The first fitting scenario included one symmetric and two asymmetric Gaussians, resulting in eight varied parameters. Typically 110 masses were populated and fitted in the experimental unsymmetrized (unmirrored) mass distributions. The chi squared per degree of freedom (χ^2/ν) as a function of proton beam energy is shown in Fig. 3. This scenario is indicated in the legend as $2+1$. Naturally the lower energies, with lower statistics, give smaller χ^2/ν, whereas at higher energies, with over 10^6 fissions, the χ^2/ν is typically between 3 and 5. The other scenarios will be presented after the $2+1$ fit parameters are discussed.

The energy dependences of these fit parameters are shown in Figs. 4(a)–4(c). The fit parameters show reasonably consistent behavior, with the symmetric probability increasing with E_p as expected. Note that the probability plateaus in the energy ranges 7–9, 13–17, and 21–25 MeV, consistent with conclusions from the raw mass spectra shown in Fig. 2. An example of a fit, for $E_p = 11$ MeV, is shown in Fig. 4(d). There the χ^2 for each point is shown by the green dashed line, with the scale shown on the right of Fig. 4(l).

Consistently, the region between the symmetric peak and the asymmetric StI peak is not well fitted, the fit being lower than experiment. The probability of the symmetric mode increases with E_p, and the width of the StI mode increases, presumably to reduce the deviation and thus the contribution of the χ^2 in this region as the relative yield here increases. Evidence for a non-Gaussian (flat-topped) symmetric mode was found in Ref. [11] at $E_p = 10.3$ and 18.0 MeV, though StI and StII appeared to be Gaussian. Our fits also suggest a flat-topped shape would be preferable, but no particular functional form or specific dependence on excitation energy was provided in Ref. [11]. A flat-topped shape can be well approximated by two offset Gaussians, inspiring the second fitting scenario described below.

2. Six Gaussian fitting

In this scenario, the mass-symmetric component was replaced by a third mass-asymmetric component (nonstandard, nonsymmetric, labeled NS in Fig. 4), giving nine fit parameters. If the mass-symmetric region could be fitted by two Gaussians with a small offset from symmetry, this fit should confirm it. This scenario indeed resulted in much lower χ^2/ν (indicated by $3+0$ in Fig. 3), and lower χ^2 near symmetry, as shown in Fig. 4(h) by the green dashed line. The NS component itself is shown in Fig. 4(h), and is clearly flat topped. The fit parameters determining the NS shape, presented in Figs. 4(e) and 4(f), have little dependence on E_p. The near-symmetric region of the NS shape becomes more rounded at higher E_p, but is far from a single Gaussian. The probability of the NS component closely matches that of the mass-symmetric component, since these are the only components that contribute at mass symmetry. This scenario gives the mean centroid of the StI and StII modes at $A = 133.8$ and 140.9, distributed with standard deviations (excluding the lowest two energies) of 0.22 and 0.28. The widths were 3.38 and 5.59, respectively, with standard deviations 0.15 and 0.24. The probability of the StI mode is consistently much smaller in this scenario [compare Figs. 4(d) and 4(h)], and has a different energy dependence, as can be seen by comparing Figs. 4(c) and 4(g).

3. Seven and more Gaussian fitting

Is the NS asymmetric component actually associated with the liquid drop fission valley (perturbed by deformed shell effects [5]), or is there a separate mass-symmetric fission

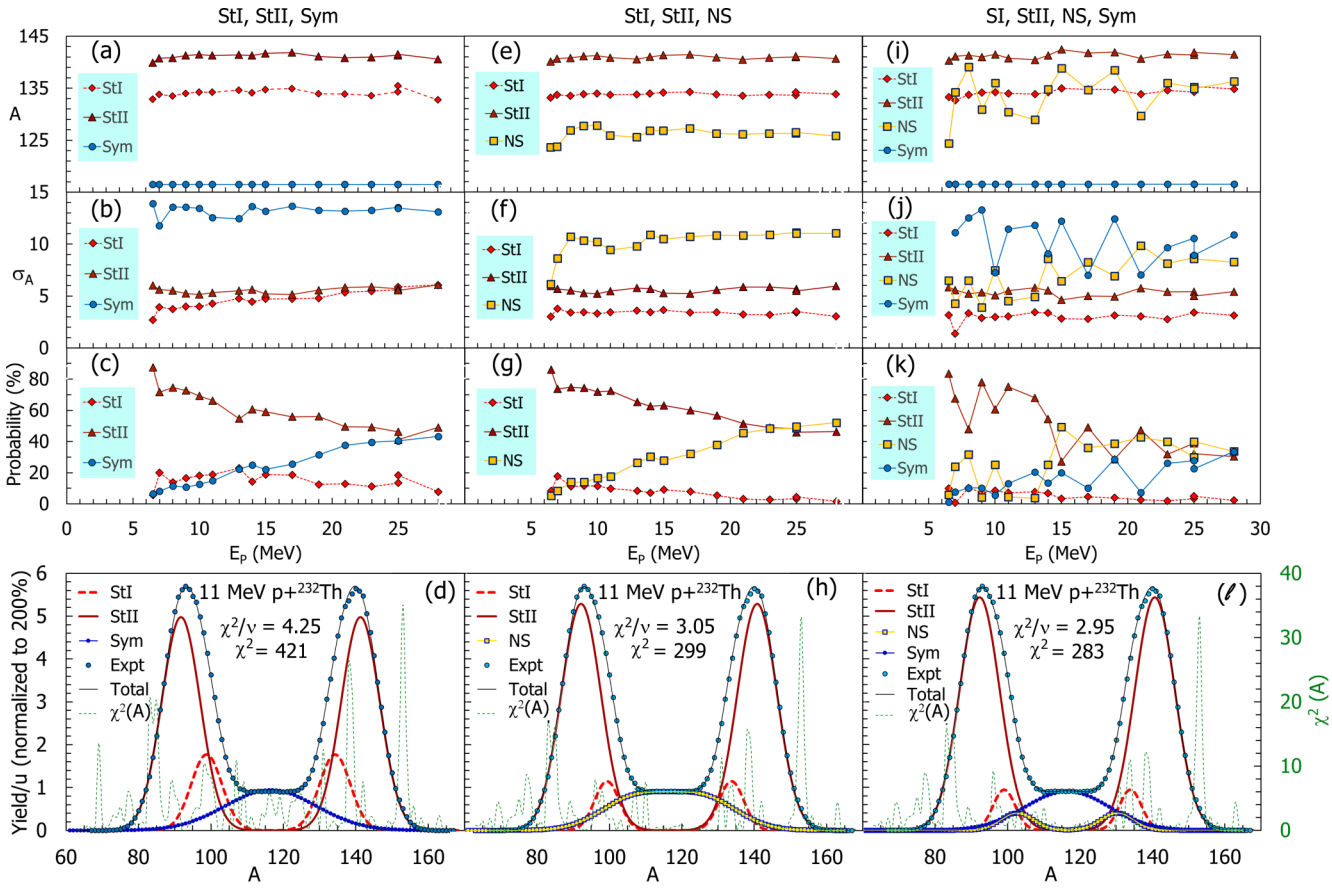

FIG. 4. The upper panels show the parameters of fits to the mass distributions with different numbers of Gaussians. They correspond to standard 1 (labeled StI), standard II (StII), symmetric (Sym), and a possible nonstandard nonsymmetric (NS) mode, as indicated. (a), (e), (i) Gaussian centroids A, (b), (f), (j) widths σ_A, and (c), (g), (k) relative areas (probability) as a function of proton energy E_p for the three scenarios tested. The scatter in the fit parameters when including three asymmetric modes and one symmetric mode is clear in panels (i), (j), and (k). The lowest panels (d), (h), (l) show the mass spectrum and associated fits for 11-MeV $p + {}^{232}$ Th. Statistical uncertainties are smaller than the point size. The contribution—$\chi^2(A)$—to the total χ^2 from each data point at mass A is shown by the dashed green lines, with the scale shown on the far right.

mode? A symmetric Gaussian was added to the fit, as well as the three mass-asymmetric modes. The results are shown in Figs. 4(i)–4(l). The centroids and widths of the StI and StII modes are reasonably stable as a function of E_p, the former averaging $A = 134.2$ and 141.3, and the latter 3.0 and 5.3, respectively. However, the centroid, width, and probability of the NS mode vary wildly. The probability of the StII mode, and the width and probability of the symmetric mode, are also unstable, as shown in Figs. 4(i)–4(k). Clearly the structure in the experimental mass distributions is insufficient to allow stable decomposition into four different modes with unconstrained parameters. The χ^2/ν values are slightly improved ($3 + 1$ label in Fig. 3), even with the increased number of fit parameters. However, the fit is not useful to define the probabilities of the StI and StII modes. Adding yet another mass-asymmetric Gaussian to the 11-MeV fit (starting close to the mass of the proposed StIII mode [9]) reduces the χ^2/ν still further, as shown in Fig. 3. However, the lowest χ^2 fit no longer even returns well-defined StI and StII modes.

4. Problems of Gaussian fitting

When fitting actinide fission mass distributions by themselves with multiple Gaussians functions, it is concluded that significant uncertainties are unavoidable. Another approach is to compare the data with a sophisticated model of fission mass distribution systematics. Comparisons with the code GEF are made in Sec. IV E. Significant disagreements in the shape of the mass distributions are seen. These preclude quantitative analysis of the experimental results making use of GEF, without modification of the code. Currently in the GEF code, the standard II mode is not represented by a Gaussian, but by a smoothed rectangular function [32]. If this represents the true nature of the mode, fitting experimental mass spectra with Gaussian functions can clearly lead to ambiguous results.

Instead of extending fitting procedures aiming to determine the probabilities of the StI and StII modes, an alternative approach has been developed, whereby the energy dependence of the mass-asymmetric peak has been characterized by purely empirical quantities. This approach has proven successful, as described below, giving new insights into the competition

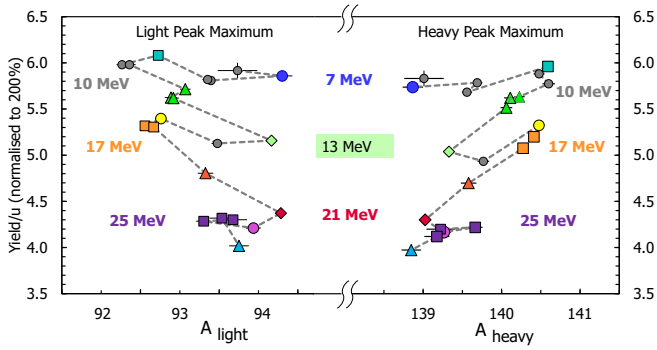

FIG. 5. The variation with beam energy of the position in mass units, and yield in percent, of the fitted maximum of the light and heavy mass-asymmetric peaks (see text). The dashed lines join data from adjacent or repeat energies. The overall reduction in yield with beam energy is largely due to the increase in the mass-symmetric fission component. The beam energies corresponding to the extrema in peak mass are indicated, color coded to the data points in this figure and in Fig. 2. The periodic variation is interpreted in terms of the low excitation energy competition between the StI and StII fission modes, and contributions from multichance fission (see text).

between StI and StII modes, and highlighting the crucial role played by multichance fission.

C. Beam energy dependence of asymmetric peak characteristics

The empirical characteristics of the mass-asymmetric peaks that have been selected are directly associated with the observation of the shifting of the asymmetric peak maximum with E_p. They are simply the yield and mass at the peaks of the distributions. These were obtained by fitting a single Gaussian function only around the top of each peak. Fitting with a third-order polynomial gave the same results, within experimental fitting uncertainties.

The correlated mass-asymmetric peak maxima, and their associated masses, are shown in Fig. 5 for all measured beam energies. The symbols are the same as in Fig. 2. Intermediate energies are shown by gray circles. Both the light peak and heavy peak (fitted independently) show essentially the same behavior. This comprises a repeated shift in the peak towards mass symmetry, then back away from mass symmetry as the beam energy increases. The amplitude of the shift decreases with increasing beam energy. The proton energies corresponding to the extrema of the oscillations are indicated. The extrema closer to mass symmetry occur at 7, 13, and 21 MeV whereas the mass-asymmetric extrema are at 10, 17, and 25 MeV. The difference in energy between the extrema increases from ≈6 to ≈8 MeV with increasing beam energy. These energy steps would be expected if the changes in the asymmetric peak were correlated with the opening up of new fission chances. This also seems to be the case for the energy dependence of the mass-symmetric mode.

Quantitative interpretation of the dependencies on beam energy needs a comparison with energy thresholds for multichance fission.

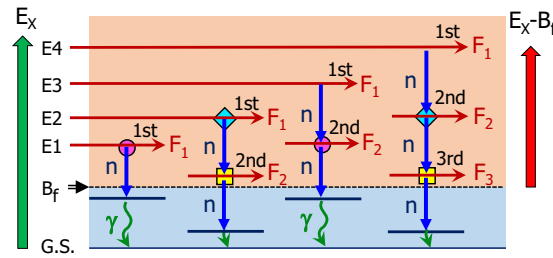

FIG. 6. Illustration of multichance fission (see text) from four different initial excitation energies $E_x = E1$–$E4$. Fission from the same E_x above the fission barrier B_f (denoted by the same colored symbols) will have the same fission mass distribution, whether resulting from first, second, or third chance fission (F_1, F_2, or F_3). The separation in *initial energy* between last chance fissions at the same final E_x will be the energy lost in emitting a neutron n (blue arrows).

D. Multichance fission and repeated changes of fission characteristics with energy

Features in the mass-symmetric yield and in the asymmetric peak characteristics have been noted that show repeated changes with beam energy, with a 6–8-MeV period. The basic reason for this is proposed to be multichance fission.

The relevant characteristics of multichance fission are illustrated schematically in Fig. 6. The orange region shows excitation energies E_x above the fission barrier B_f where fission (F) is likely. The blue region below B_f has negligible fission, so neutron evaporation (n) and γ-ray emission ($\boldsymbol{\gamma}$) dominate. The colored circles, squares, and diamonds indicate where the decision to fission or emit a neutron is made. The same symbol indicates the same E_x, whether resulting from first, second, or third chance fission (F_1, F_2, or F_3). For simplicity, it is assumed that the fission modes after neutron evaporation do not change, which is reasonable for a small number of emitted neutrons. If different fission modes have different B_f, the total fission mass distribution will change rapidly with E_x at energies just above B_f. In the diagram, the initial E_x values where this may occur are at $E2$ and $E4$, for second and third chance fission, respectively. In proton reactions, the fusion barrier in practice prevents fission mass distribution measurements lower than $E1$. This prevents measurements of first chance fission mass distributions in this crucial energy region using proton beams.

As long as the probability of last chance fission is significant [7], the total (measured) fission mass distribution will change periodically. The E_x spacing ($E3 - E1$ or $E4 - E2$) will correspond to the energy lost by emitting a neutron (blue arrows). This energy cost is the sum of the neutron binding energy (between 5.5 and 6.8 MeV for the relevant Pa nuclei) and the neutron kinetic energy. The neutron kinetic energy distribution has a mean of approximately twice the nuclear temperature. Thus an energy period for changes in the fission mass spectra of 6–8 MeV is consistent with multichance fission being the cause.

The period, amplitude, and nature of the changes in the fission mass spectrum carry information about both the change in mass distribution with E_x, and the probabilities of last chance fission. To disentangle these would need a

comprehensive model of fission. Multichance fission is modeled in the Monte Carlo GEF code [32]. It will be instructive to make comparisons of features of the experimental mass distributions with GEF calculations.

E. Comparison with mass distributions calculated by GEF

Before direct comparison with GEF calculations, measures have to be taken to ensure the calculated spectra are equivalent to those measured.

GEF calculates fragment masses at scission. These masses account for the mass changes at scission resulting from neutron emission from the fissioning system before scission. This emission is the origin of multichance fission, thus the scission mass number differs by 1 for fission from the first chance, second chance, etc. In the experimental data, there is no information on the fission chance of a given fission event. As previously noted, the $2v$ experimental fragment masses at scission can only be determined by assuming the scission mass. To avoid ambiguity, in this paper this was taken to be the compound nucleus (first chance fission) mass.

To allow the correct comparison of our experimental data with GEF, the event-by-event GEF fragment masses have been converted into a mass ratio, and then the equivalent first chance fission masses determined assuming the scission mass to be the compound nucleus mass. These mass distributions have been smoothed with a Gaussian of standard deviation 1.5 u to eliminate spurious structures arising from integer mass numbers. This also simulates fragment velocity dispersion due to neutron evaporation from the fission fragments (see Appendix A).

These procedures make the GEF calculations closely equivalent to the experimental results. GEF also includes effects of preequilibrium nucleon emission when the proton beam energy is provided as input to the code [32]. This spreads the distribution of initial equilibrated excitation energies to a lower mean value. Insofar as the model of preequilibrium emission matches reality, the experiment and calculations should be as nearly equivalent as possible.

Experimental mass distributions are compared in Fig. 7 (left) with calculations from GEF (right) for the indicated proton beam energies. The data labeled G13 are from a measurement using the $2v$ technique by Gikal *et al.* [5], for 13-MeV protons. The main characteristics are close to our 13-MeV data. It can be seen from Fig. 7 that the GEF calculations do remarkably well in matching the experimental results. Only in two aspects do they significantly disagree.

The first disagreement is in the mass-symmetric component, which in the GEF calculations is clearly separated by a valley from the mass-asymmetric peaks. In contrast, both experimental measurements for 13 MeV are in excellent agreement, and show an almost flat distribution around symmetry, as do many other measurements (e.g., Ref. [11] and references therein). More extensive indications of the consistency of the present measurements with previous results are discussed in Sec. IV G. It is concluded that the disagreement with GEF is not of instrumental origin. Thus some feature seems to be missing in this mass region in the GEF model.

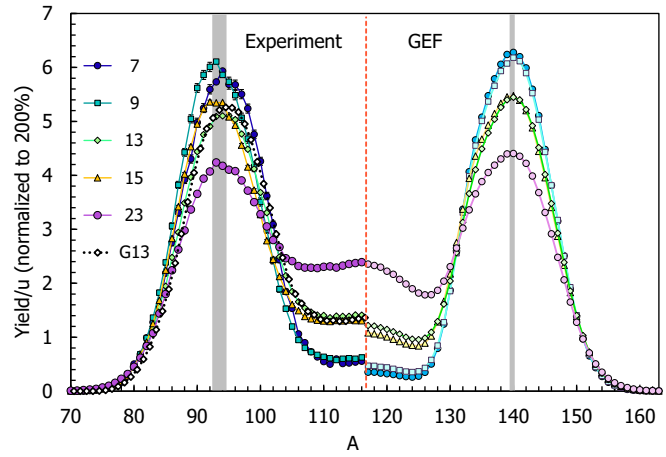

FIG. 7. Experimental light fragment mass distributions (left) at the selected proton beam energies (as indicated), together with GEF calculations for the complementary heavy fragment at the same incident proton energies. G13 refers to experimental data from Ref. [5] at 13 MeV. The agreement is quite good, but a number of discrepancies are seen: (i) the GEF mass-symmetric yield is more peaked at symmetry and (ii) the GEF mass-asymmetric peak shows very little variation in peak position compared with experiment, as indicated by the width of the underlying gray bands).

Possible physical explanations of this disagreement include (i) that the superlong mode has a much wider mass distribution than assumed in GEF; (ii) that the superlong mode is not mass symmetric, instead consisting of two overlapping Gaussians displaced from mass symmetry; and (iii) that there is an additional mass-asymmetric mode filling the dip seen in the GEF calculations between the mass-symmetric peak and the strong mass-asymmetric peak.

Fitting the mass distributions with Gaussians was not able to give a definitive answer, though it could be concluded that Gaussian distributions for the SL, StI, and StII modes, even with unconstrained parameters, could not provide a good fit to the experimental data. Additional information from high statistics correlated mass and TKE distributions can help to resolve this problem [5,11,12], but is not within the scope of this paper.

The second disagreement between GEF and experiment is in the movement with energy of the mass at the maximum yield of the mass-asymmetric fission peak. The gray band underlying the experimental distributions Fig. 7 (left side) indicates the range of peak masses from experiment. The band on the right highlights the minimal changes in peak mass from the GEF calculations. The reason for changes in the mass at the peak yield should be associated with changes in the relative probability of the standard I and standard II modes. The fits to the present mass distributions in Sec. IV B suggest they should be centered around $A \simeq 134$ and $\simeq 141$, respectively.

The experimental observation of significant changes in peak mass indicates (i) changes in the relative probability of StI and StII with excitation energy and (ii) that these changes are larger than those calculated in GEF. These points are discussed in detail below.

F. Excitation energy dependence of the mass of the asymmetric peak maximum

To interpret fission mass distribution characteristics in terms of multichance fission, excitation energy E_x is the key variable, rather than proton beam energy E_p. This is because each fission chance has a threshold excitation energy resulting from the sum of the appropriate fission barrier and the binding energies of the emitted neutrons.

In the case of proton-induced fission, the (generally) high velocity of protons causes preequilibrium nucleon emission with non-negligible probability before the compound nucleus is thermalized/equilibrated. Such emission results in the excitation energy distribution consisting of two components. The first corresponds to complete fusion at $E_x = E_p^{\text{c.m.}} + Q_{\text{fus}}$, where $E_p^{\text{c.m.}}$ is the center-of-mass energy and Q_{fus} is the fusion Q value $= 5.247$ MeV in this reaction. The second component comprises a distribution with reduced excitation energy, resulting from the distribution of energies carried away by preequilibrium particle emission.

GEF calculations can be carried out for defined proton beam energy, or for a defined excitation energy. The latter shows most clearly structures in observables arising from multichance fission. For the former, which include preequilibrium emission, these structures are smeared out by the distribution of initial excitation energies. The degree of smearing is determined by the characteristics of the calculated preequilibrium emission distributions. Results from both types of calculation are presented.

GEF calculations of the relative probabilities of different fission chances are shown in Fig. 8(a), as a function of E_x. The larger colored symbols joined by full lines correspond to calculations for defined proton energies. They are plotted at $E_x = E_p^{\text{c.m.}} + Q_{\text{fus}}$, which is the maximum E_x populated in the reaction, but, as discussed above, lower E_x components are present. These calculations are labeled GEF Ep in the panels of Fig. 8. The smaller symbols joined by dashed lines are calculated for single initial E_x values, and are labeled GEF Ex.

The two types of calculation show similar behavior, with the probability of each fission chance starting near the threshold energy expected from the sum of the neutron binding energies and the appropriate fission barrier (arrows on the E_x axis). As expected the higher fission chances rise more slowly with E_x for the calculations including preequilibrium emission. The shaded bands show the regions where low excitation energy fission will be present, above the E_x threshold for each fission chance. Any feature in the experiment associated with E_x values just above the fission threshold should be seen within these bands.

The fission angular anisotropy is known experimentally [34] to increase at low E_x. Our experimental values, shown in Fig. 8(b), indeed rise in these energy bands, in agreement with expectations.

The experimental masses at the asymmetric fission peak maxima are shown in Fig. 8(c). The masses from the measured light fragment peak have been mirrored to the corresponding heavy fragment masses. These independent measurements are in quite good quantitative agreement. Two independent measurements using the $2v$ method are also shown, from Nagame

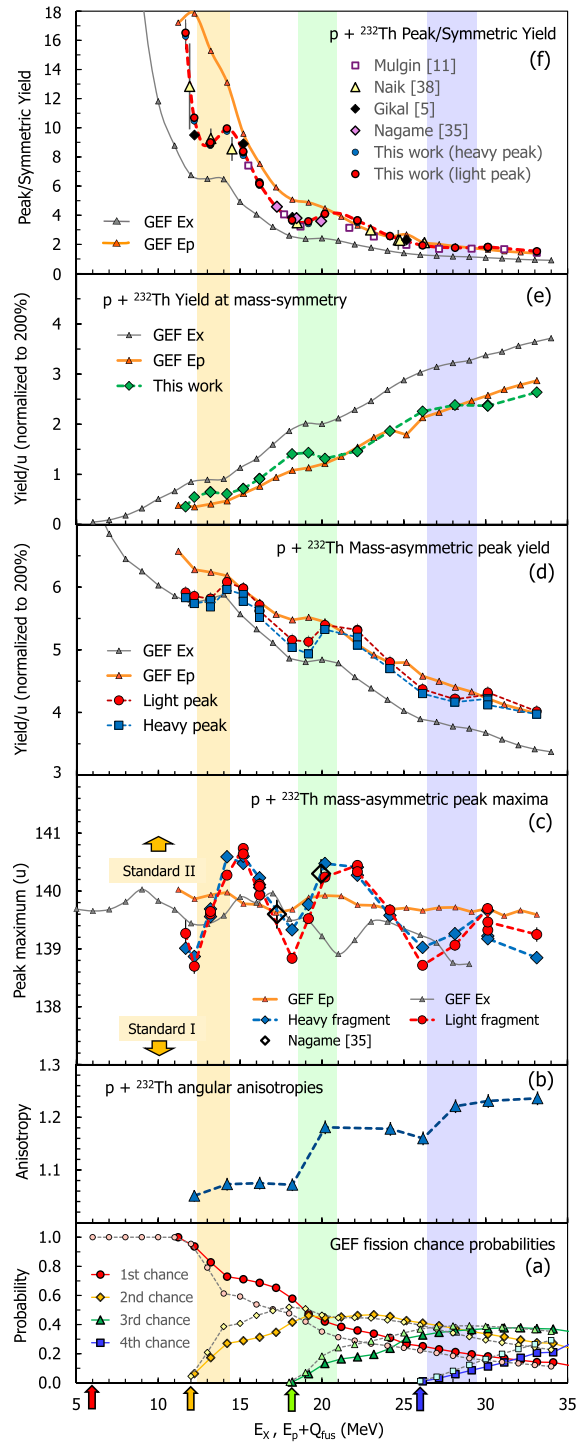

FIG. 8. (a) GEF calculations of the relative probabilities of multichance fission, calculated for unique initial excitation energies E_x (small symbols joined by dotted lines) and for proton beam energies plotted at the excitation energies corresponding to no preequilibrium emission ($E_p^{\text{c.m.}} + Q_{\text{fus}}$—see text). Thresholds for each fission chance are indicated by color-coded arrows. Shaded bands correspond to just-above-threshold energies for second, third, and fourth chance fission. All the experimental observables in the panels above show features in these regions. Comparisons with GEF calculations for initial excitation energies E_x and initial proton energies E_p are given (see text).

et al. in 1996 [35]. Despite larger estimated uncertainties arising from reading the data from the published figure, they are in good agreement with the present results.

The mass at the maximum peak yield is lowest ($A \simeq 139$) at $E_x \simeq 12$, 18, and 26 MeV. Here the probability of the StI mode (centered at $A \simeq 134$ according to our fits) must be highest. Above these energies the peak mass rises rapidly, reaching a maximum of $A \simeq 140.5$, close to the fitted StII centroid of $A \simeq 141$. From the lowest mass found at $E_x = 12$ MeV (above which the second chance probability starts to rise), the maximum mass is reached by 15 MeV. According to the GEF calculations, second chance fission rises from 0 to 30–40% in this energy range, indicated by the underlying yellow band in Fig. 8. The mean excitation energy of second chance fission will rise over this energy range, but by less than this energy range itself, because of the kinetic energy of the emitted neutron. It is thus concluded that the relative probabilities of StI and StII must change very rapidly above the fission threshold energy.

Third chance fission is calculated to have its threshold at 18 MeV, above which the second rise in the mass of the peak maximum is found to occur (green band). Similarly fourth chance fission rises from 26 MeV (blue band), corresponding to another (weaker) rise in the mass at the peak maximum. These results reinforce the conclusion from the observations above the second chance fission threshold energy.

To summarize, in three E_x ranges where low E_x fission recurs due to crossing last chance fission thresholds, the mass-asymmetric peak maximum shows a similar increase in mass. Where the excitation energy of last chance fission is less than 3 MeV above the lowest fission barrier, the contribution of the StII mode increases with E_x. At more than 3 MeV, the StII contribution decreases relative to the StI mode, which continues to increase in relative probability until the next energy threshold for last chance fission, at 6 MeV or more. The simplest explanation is that the StI and StII modes have different fission thresholds (fission barrier heights), with the StII mode having the lower barrier, but as E_x increases above the StI barrier StI continually increases in probability. The lowest mass of the asymmetric peak maximum is just below $A = 139$ at $E_x \approx 12$ MeV, where only first chance fission contributes. Taking the StI and StII peaks to be at $A = 134$ and 141, respectively, assuming the widths of the modes to be the same implies a StI/StII probability ratio at this E_x of ≈40%. A narrower StI width would reduce this ratio in proportion, but nevertheless, the fraction of StI appears to be substantial.

How do these experimental results compare with GEF calculations? These are also shown in Fig. 8(c). Calculations specifying the proton energy (labeled GEF Ep, each calculation for 2×10^6 fission events) are indicated by orange triangles joined by the thick curve. As anticipated from Fig. 7, the variation in peak mass with E_p is minimal compared with experiment. The distribution of E_x for each E_p resulting from preequilibrium emission will contribute to the lack of variation, but the dispersion from this effect must be present in the experimental results too. Calculations for single initial E_x (labeled GEF Ex) are shown by the smaller triangles joined by the thin line. They show a larger variation with E_x, but the amplitude and phase of the variations do not match experiment.[1]

To conclude, GEF does not reproduce the change in the relative probabilities of the StI and StII fission modes as a function of excitation energy in $p + ^{232}$ Th reactions. In the GEF code, the StII fission barrier is taken to be lower than the StI barrier, which is in agreement with the empirical behavior. However, the detailed energy dependence of calculated observables resulting from this does not match experiment, which suggests a much larger contribution from the StI mode, and a larger influence of E_x on the relative probabilities of StI and StII than is calculated by GEF.

To simplify the comparison of experiment and calculation, only the mass at the maximum of the mass-asymmetric peak has been compared. To obtain a better match with the experimental changes in the mass-asymmetric peak, it would be valuable to evaluate the goodness of fit to some or all of the experimental asymmetric peak. However, if attempting to compare the whole mass spectrum, the quality of fit would probably be dominated by the much larger discrepancy seen for masses between symmetry and the rise of the mass-asymmetric peak, as discussed in Sec. IV E.

The current data on the scission mass at the asymmetric peak maximum agree with the two results of Nagame *et al.* [35], obtained with the $2v$ method. The data of Gikal *et al.* [5] are typically within 0.5 mass units of the present results. There the scission mass was corrected for prescission neutron evaporation, measured [5] to be 0.5 ± 0.2 neutrons at $E_p = 13$ MeV. Thus the mass discrepancy reduces to only 0.25, which is likely within systematic uncertainties resulting from fragment energy loss corrections (see Appendix B). Other measurements of mass spectra have used the $2E$ method, or decay counting. These determine masses after neutron evaporation from the fragments, and comparison would require the complication of attempting corrections for neutron evaporation.

Almost all measurements can be compared through an empirical quantity extracted in many measurements. This is the ratio of the yield at the maximum of the asymmetric peak to the yield at mass symmetry. This is often called the peak to valley (P/V) ratio. It is expected to be almost unaffected by neutron evaporation. Results from several previous experiments are compared in the next section. This provides strong validation of the current results, and shows excellent consistency among the previous results. Significant repeated structures are clearly present in the energy dependence of P/V, which to our knowledge is presented for the first time.

G. Energy dependence of mass-asymmetric peak to mass-symmetric yields

Before evaluating and comparing peak to valley ratios, the energy dependence of the two components of P/V from the

[1]The mean is artificially higher for GEF Ep calculations because of the mass lost by preequilibrium emission, combined with the mass renormalization of the GEF calculations to match the experimental assumption that the mass at scission is the compound nucleus mass.

current experiments will be discussed. This will clarify the interpretation of the energy dependence of the P/V ratio.

Peak yields are shown in Fig. 8(d) as a function of energy. As noted, the light and heavy peak yields show a slight systematic difference, of a few percent. Both show a consistent energy dependence, with dips in yield at the threshold of each fission chance (low energy side of the colored bands), and peaks a few MeV higher (upper edge of the colored bands). These correlate strongly with the change in the mass at the maximum of the asymmetric peak shown in Fig. 8(c). This correlation is to be expected, since when the mass at the maximum is closer to the average of the StI and StII masses ($\simeq$137.5) the mass-asymmetric peak will be wide, and thus the peak height will be reduced due to the normalization of the mass spectra to 200%. Conversely when the peak mass is closest to the StII mass, the asymmetric peak will be narrower and higher.

Despite having little difference in asymmetric peak shape with energy, the GEF calculations also show plateaus (though not peaks) in the same energy range. The origin of this feature is related to the energy dependence of the *mass-symmetric* mode, discussed in more detail below. Because of the overall normalization of all modes to 200%, physical processes affecting the symmetric yields will affect the peak yields, and vice versa.

The yield at mass symmetry is shown in Fig. 8(e). The basic expectation is that the yield of the mass-symmetric mode (and thus the yield at mass symmetry) will increase with excitation energy. This is because the mass-asymmetric modes exist because of shell effects which are attenuated as excitation energy increases. In contrast the mass-symmetric mode is generally identified with the liquid drop model fission barrier, which does not change rapidly with E_x.

The experimental data show an overall rise, but with plateaus within the shaded bands, possibly even falling at the upper edge of the shaded bands. The plateaus are clearly present in the GEF Ex calculations, and in attenuated form in the GEF Ep calculations. The explanation is again multichance fission. At the low energy edge of the bands, low E_x fission starts to reappear due to passing the energy threshold for a new fission chance. Low E_x corresponds to a lower probability of the mass-symmetric fission mode, so the yield at mass symmetry no longer rises. Depending on the probability of the new last chance fission, the symmetric yield could even fall as E_x rises above the threshold.

The GEF Ep calculations are quite successful in describing the overall trends of the symmetric yield, but the steps related to multichance fission are very much attenuated compared with experiment. This suggests that the calculated effect of preequilibrium emission on the excitation energy spectrum is overestimated, and/or the last chance fission probabilities in GEF are lower than found in reality. Comparison of xn evaporation residue excitation functions [36,37] with GEF calculations should provide insight into this question.

The features seen in the energy dependence of the experimental yields both at the asymmetric peak maxima and at mass symmetry have been explained in terms of physical effects largely related to multichance fission and StI/StII competition. Now the peak/valley ratios can be more easily interpreted, and compared with other measurements and with the GEF calculations. These are all shown in Fig. 8(f).

The P/V results of the present paper are indicated by red circles (light fragment peak) and blue circles (heavy fragment peak). On this scale, these two independent results generally overlap completely. The thick dashed red curve joins the red points and guides the eye. The agreement with previous experimental results is remarkably good. Measurements from direct detection of fission fragments cover $2E$ measurements (labeled Mulgin *et al.* [11]) and $2v$ measurements (labeled Gikal *et al.* [5] and Nagame *et al.* [35]). The values from the tabulation of Naik *et al.* in 2013 [38] are generally from decay counting. Without the present data, taken with fine energy steps, the structure in the P/V ratio would not be readily apparent. Indeed, from data with a 2-MeV energy step, Mulgin *et al.* concluded [11] that the ratio of the StI and StII modes was independent of energy, and the P/V ratio was smooth and featureless. In contrast, decay counting measurements [39] with fine energy steps did identify a structure in P/V at $E_x \approx 21$ MeV ($E_p \approx 16$ MeV), and it was associated with the onset of third chance fission, as it is here. For the ^{232}Th (n, f) reaction, a feature in the asymmetric peak characteristics, and in P/V, at $E_x \approx 12$ MeV was identified as a GDR effect [40]. The onset of second chance fission may be expected to play a role in that reaction also.

GEF calculations show structures in qualitative agreement with experiment. Quantitatively, the multichance fission and excitation energy dependence of competition between StI and StII modes does not seem to match with experiment.

The P/V ratio is perhaps the most robust experimental characterization of mass distributions in the neutron-rich Th-Cm region. The origins of repeating structures in the P/V ratio as a function of energy have been identified from the physical processes affecting both the peak yield and the symmetric yield. Variables identified as affecting the ratio include (i) the detailed energy dependence of the StI to StII ratio near threshold, (ii) the energies of onset and the probabilities of successive last chance fission, (iii) the E_x dependence of the mass-symmetric mode characteristics folded with the multichance symmetric fission probability distributions [39], and (iv) the distribution of E_x resulting from preequilibrium emission.

This paper has shown that the excitation energy dependence of the symmetric fission probability appears to be strongly affected by multichance fission. Thus extracting the intrinsic dependence on E_x of the competition between symmetric and asymmetric fission is reliant on knowing the contributions from different fission chances. This intrinsic dependence in turn gives insights into the attenuation of shell effects with E_x, a fundamental property of nuclei. A quantitative model reproducing all the experimental behaviors should be able to give insights into these issues, and GEF would seem to be a good starting point. The experimental results suggest that the physics determining the detailed excitation energy dependence of fission mass spectra still needs development.

V. SUMMARY AND CONCLUSIONS

New measurements of fission have been carried out for the $p + ^{232}$ Th reaction at 15 beam energies from 6.5 to 28 MeV,

to investigate the dependence of the relative probabilities of the standard I and standard II mass-asymmetric fission modes as a function of excitation energy. For fission modes like these, caused by shell structure, their variation with excitation energy gives important guidance to models.

The new experimental analysis method used, that determines fission mass spectra from time difference information alone, has been rigorously tested and validated. It requires information from previous measurements or calculations of the mean fission total kinetic energy as a function of mass split. The results are shown to be not very sensitive to this input. Time difference mass distributions are essentially identical to those extracted using the double velocity ($2v$) method applied to identical data sets.

Visual inspection of the mass distributions reveals *periodic* structure in the energy dependence of the symmetric yield and in the mass and probability at the peak of the mass-asymmetric component. This suggests a significant influence of multichance fission in the structure of the mass distributions.

Fitting the mass distributions with unconstrained Gaussian functions failed to give good fits and stable Gaussian fit parameters simultaneously. External constraints, from experimental mass-TKE distributions or firmly based theoretical expectations, are needed to extract absolute probabilities of different fission modes by fitting. This will be addressed in a subsequent paper.

Comparison with mass distributions calculated using the code GEF shows only two significant discrepancies. The first is that experimental mass distributions between the two mass-asymmetric peaks are much flatter than those calculated, which assume a Gaussian form. This experiment is in agreement with many previous works. Our fits, and previous work of others [11], both suggest that the mass-symmetric component is flat topped, rather than Gaussian in shape. This suggests shell structure is also affecting the symmetric mode [11]. The second disagreement is that the mass at the peak of the asymmetric component changes with energy much more in the experiment than in the GEF calculations. This must reflect a strong dependence with excitation energy of the relative probability of the StI and StII modes, with StI having significant probability.

Plotting empirical observables as a function of excitation energy (assuming complete fusion) reveals repeated changes just above successive energy thresholds for last chance fission. These observables are the angular anisotropy, the yield at mass symmetry, the asymmetric peak height and the mass at the peak maximum, and a combined variable: the ratio of peak yield to symmetric yield (referred to as peak/valley—P/V). The GEF calculations show much weaker dependence on excitation energy, particularly when they include the dispersive effect of preequilibrium emission of nucleons before compound nucleus formation.

These correlations lead to several conclusions.

(1) The StII fission barrier appears to be lower than the StI barrier, which is also the case in the GEF code.

(2) Above the StI fission barrier, the StI fission probability appears to rise faster and to higher values than in the GEF calculations.

(3) Last chance fission appears to have a higher probability than in the GEF calculations, particularly those that include preequilibrium emission.

(4) Preequilibrium emission probabilities at low energies may be smaller than those calculated in GEF, supported by the experimental neutron angular correlation measurements of Ref. [5].

(5) The peak to symmetric yield ratio P/V is the most robust experimental observable, and many previous measurements are in excellent agreement with the present paper.

(6) Distinct structures on a ≈2-MeV energy scale in the P/V ratio suggest a significant probability of last chance fission, even at E_x up to 30 MeV. They repeat every 6–8 MeV, through decreasing in amplitude at higher energy. This behavior can be attributed to the energy cost and increased energy spread associated with successive neutron emissions, and the expected decreasing contribution from last chance fission with increasing E_x.

The simultaneous description of all experimental variables presented could perhaps be achieved by empirical adjustment of parameters within the GEF model. This task is, however, beyond the scope of the present paper.

The results show that many features of the experimental fission mass spectra, even at excitation energies up to 30 MeV, are affected by last chance fission. This occurs in the excitation energy range from around 6 to 12 MeV. It would be extremely useful to measure directly precise mass distributions in this energy range to pin down barrier heights, and to help to develop empirical and fundamental models describing multichance fission. These measurements cannot be obtained with good statistics through proton fusion, since the beam energies are far below the fusion barrier. Transfer reactions would allow population in this energy region with much higher cross sections. Such high statistics mass distribution measurements (ideally based on $2v$ measurements) are strongly encouraged.

ACKNOWLEDGMENTS

The authors acknowledge helpful advice from Dr. K.-H. Schmidt in processing GEF outputs to meet the requirements of this work. Financial support from Australian Research Council Grants No. DP200100601, No. DP190101442, No. DP190100256, No. DP170102318, and No. DP160101254 is acknowledged. The Australian Federal Government National Collaborative Research Infrastructure Strategy program supported operations of the ANU Heavy Ion Accelerator Facility through the HIA capability. This work was partially supported by Japan Society for the Promotion of Science KAKENHI Grant No. JP19002005. Work at Lawrence Livermore National Laboratory (LLNL) was performed under the auspices of the U.S. Department of Energy by LLNL under Contract No. DE-AC52-07NA27344. B.M.A.S.-B., J.B., and L.T.B. acknowledge the support of the Australian Government Research Training Program.

APPENDIX A: BENCHMARKING THE TIME DIFFERENCE METHOD

The time difference method for fission of systems with small or zero center-of-mass velocities was presented in

Ref. [25]. To test the accuracy of the method, a fission mass measurement using time difference should be compared with a high quality measurement made using another method (e.g., double energy $2E$ or double velocity $2v$) that does not need to use external data on the relative fission fragment c.m. velocities (this *external* information *is* required by this time difference method). A comparison was already made in Ref. [25], where good agreement was obtained for a relatively narrow mass distribution previously measured by the double energy method. As shown there, the full expression for the mass ratio M_R at scission can be approximated by the equation

$$M_R \cong 0.5 - \frac{K\Delta T}{8d} \tag{A1}$$

where K is the relative velocity of the two fission fragments in the c.m. frame, and ΔT is the time difference between the fragments measured in two detectors both at distance d from the fission event. In practice, for a given value of M_R, only the mean value $\langle K \rangle$ can be provided—if event-by-event information were available, there would be no need to apply the time difference method. For small mass asymmetry between the two fragments ΔT is small, and so the sensitivity to K is also small. A more severe test would be for a distribution extending to large mass asymmetry, also having significant structure in the mass distribution.

1. Spontaneous fission of ^{248}Cm

Spontaneous fission of ^{248}Cm is a good candidate, with very low yield at mass symmetry, a mass-asymmetric peak with structure, and yield extending outside $M_R = 0.35$ and 0.65. Experimental mass distributions exist in the literature, the most extensively described that we are aware of being from Unik *et al.* [17]. Measured by the $2E$ method, in principle it is the mass split of the fragments after neutron evaporation that are obtained by this method. However, in Ref. [17] the data were iteratively corrected event by event for postscission neutron emission as well as energy loss in the target. This allows comparison with the present time difference measurement which provides the mass split at scission. The mass distribution of Unik *et al.* was extracted from the data presented on a linear scale in Fig. 2 of Ref. [17]. Digitized values of yield will have a scanning uncertainty introduced, estimated to correspond to an uncertainty in the absolute yield of ≈0.015 % per mass unit. Thus insignificant uncertainty was introduced for absolute yield per mass unit above 1% per mass unit.

In our analysis method for time difference data, the mean relative fragment velocity as a function of mass split needs to be provided. This was obtained from the experimental data of Unik *et al.* presented in Ref. [17] for ^{246}Cm (data for ^{248}Cm were not presented). The mass distributions for ^{248}Cm and ^{246}Cm were measured to be very similar, so the TKEs should also be similar. Fragment energy loss in the target and backing were corrected using energy losses calculated from the equations of Knyazheva *et al.* [43], which describe experimental measurements specifically for fission fragments. Both the mass split dependence of fragment velocities and the effects of energy loss were corrected for iteratively, event by event. The only parameter varied in the analysis was the value of the time difference offset, which was adjusted to obtain a mean fragment mass ratio of exactly 0.5. The fragment masses were obtained assuming the mass number A at scission was 248.

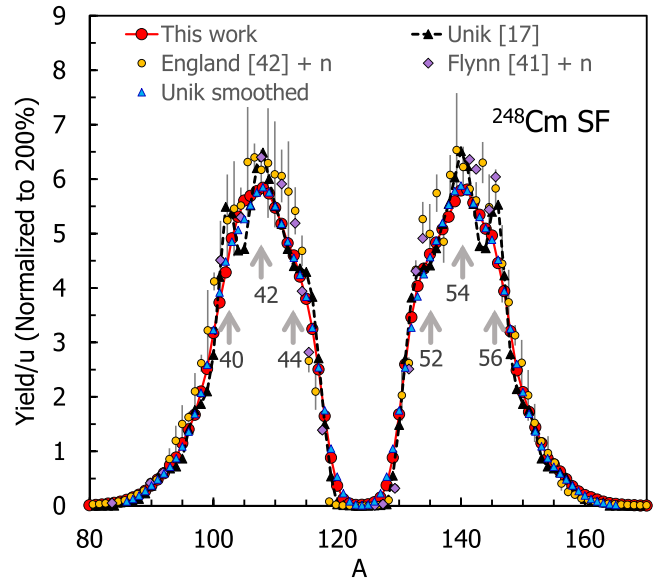

FIG. 9. Mass spectra at scission for spontaneous fission of ^{248}Cm. The yield scale is in percent, where the full distribution has been normalized to 200%. The data from Flynn *et al.* [41] and England and Rider [42] are mainly from decay counting, corrected for postscission neutron emission (see text). The data from Unik *et al.* [17] shown by black triangles had originally been deconvoluted [17] (to account for mass dispersion caused by neutron emission from the fragments) and mirrored about the symmetric mass split ($A = 124$). The mass spectra from the current paper (red circles) using the time difference method are unmirrored and not deconvoluted. Convoluting the Unik *et al.* data with a standard deviation of 1.8 u (blue triangles) gives good agreement with the current paper. This implies the standard deviation of the mass resolution in the current paper is ≈0.8 u (see text).

The scanned mass spectrum as presented by Unik *et al.* is shown in Fig. 9 and (in logarithmic scale) in Fig. 10 by black triangles joined by a dashed curve. It shows significant structures, correlated with even fragment charges (gray arrows). These arrows for the heavy peak correspond to $A = (Z + 0.3)A_{CN}/Z_{CN}$, and are complementary for the light peak. The mass distribution presented had been obtained in Ref. [17] from the raw distribution (not presented there) by correcting for (deconvoluting) the calculated effects of mass smoothing (dispersion) caused by neutron emission from the fission fragments. The claimed instrumental mass precision was 0.2 u, with the possibility also of systematic uncertainty arising from the Si detector energy calibration. The calculated mass number smoothing standard deviations (σ_A) resulting from neutron evaporation ranged from 1.22 to 1.78 for fissioning systems between ^{229}Th and ^{254}Fm.

Figures 9 and 10 also show mass distributions for ^{248}Cm spontaneous fission determined by decay counting [41,42]. We have corrected these by the mean prompt neutron mul-

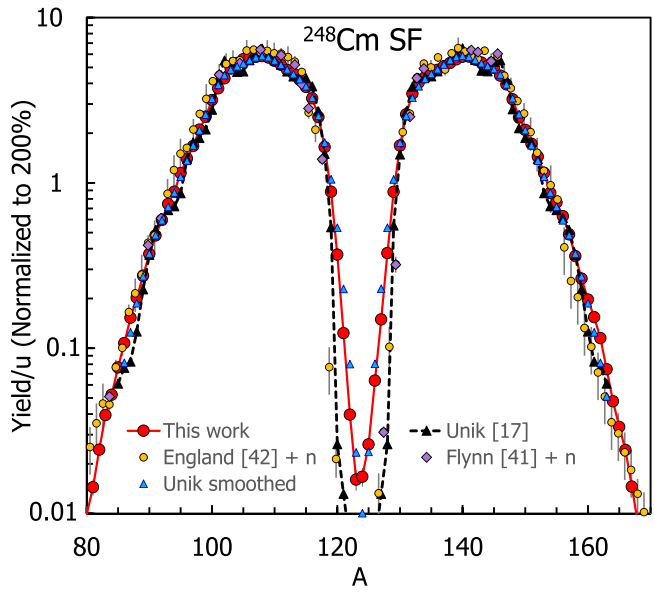

FIG. 10. The same as Fig. 9, but with a logarithmic yield scale.

tiplicity [44] as a function of fragment mass to obtain the scission masses, indicated by diamonds and circles, respectively. Over the full mass range, the agreement with Unik *et al.* is reasonable, given the large assigned error bars. The even-Z structure is not as obvious, likely also associated with the experimental uncertainties. The yield at mass symmetry is well defined, having no smoothing effect due to mass resolution. This gives a peak/valley ratio of about 4000.

Our ^{248}Cm mass spectrum is shown in Figs. 9 and 10 by red circles. Overall, the agreement with previous work is good. Our experimental peak/valley ratio is 320 for one detector pair, and 480 for the other. The spectra show the sum of the mass spectra from both detector pairs, and are not mirrored—the mass of the fragment detected in the backward angle detectors is presented. Since the spectrum shown by Unik *et al.* had been deconvoluted to compensate for dispersion from fragment neutron emission, to compare with our experiment, we have reconvoluted (smoothed with a Gaussian distribution) the mass distribution presented by Unik *et al.*, shown by blue triangles. To obtain the best agreement with our data required smoothing with σ_A of 1.8. The agreement in mean mass and structure is excellent. The mean mass of the re-convoluted heavy fragment peak ($125 \leqslant A \leqslant 153$) of Unik *et al.* is 140.17, whereas the present data gave 140.37, using the fission fragment energy loss formula of Ref. [43]. The effect of a different energy loss calculation (for the $p + ^{232}$ Th measurements) is discussed in Appendix B.

2. Instrumental mass resolution

The instrumental mass resolution of the present paper can be estimated by comparing the deconvolution width applied in Ref. [17] to the convolution width we applied to match our measurement. The deconvolution width applied in Ref. [17] is expected to depend on the mean number of neutrons emitted. Figure 5 of Ref. [17] shows that ^{248}Cm is in the higher range of neutron multiplicity, and so should be closer to the upper (1.78) than the lower limit (1.22) in σ_A. Assuming a deconvolution σ_A of 1.6 was applied in Ref. [17], the convolution width of 1.8 that matched the present results implies an experimental contribution to the mass number resolution in the current experiment of $\approx$0.8 ($\sqrt{1.8^2 - 1.6^2}$). Since the deconvolution width actually applied is only estimated, this value has considerable uncertainty.

Some known experimental contributions in the present measurements can be evaluated. According to Eq. (A1), a contribution to the resolution from the time difference method will come from the fact that K takes a distribution of values around the mean value that is used for each mass split. This is estimated to contribute only 0.2 u for masses near the asymmetric mass peak. Another contribution will come from fission occurring at all depths in the Cm material. Based on the measured thickness, this is calculated to contribute an rms mass width of 0.3 u. The largest contribution is likely to come from the experimental time resolution, i.e., the spread in time difference between the large area MWPC detectors. From Eq. (A1), a standard deviation of the resolution in time difference of 200 ps (corresponding to an individual detector time resolution of 140 ps) would give a σ_A of 0.75 at the asymmetric mass peak position. This is not close to the limit of time resolution of the time to digital converter that was used (97 ps between channels). Adding these contributions in quadrature results in an instrumental resolution $\sigma_A = 0.8$. Given the 1000-cm^2 area of each large MWPC fission detector, this resolution is quite satisfactory.

It is concluded that the fission mass resolution depends mainly on neutron emission from the fragments, with the time resolution of the detectors making a smaller contribution. The approximation in the time difference method of taking mean fragment velocities for each mass split rather than actual velocities does not make a significant contribution to the mass resolution. Appendix B addresses quantitatively energy loss corrections and less accurate treatments of fragment velocities within the time difference method.

APPENDIX B: SENSITIVITY OF FISSION MASS SPECTRA TO EXTERNAL INPUTS

The time difference method requires as input the relative velocities in the center-of-mass frame (K) as a function of the mass ratio of fragment pairs. These can be determined from the TKE as a function of mass split, making use of conservation of momentum. The TKE information could come from models, or from prior experiments.

Corrections for energy losses of fragments in the target material and its supporting backing are required for both the time difference and absolute time ($2v$) methods. The sensitivity of the mass spectra to these inputs is presented below.

1. Dependence of mass spectra on TKE input

To test the sensitivity of the time difference method to the TKE or $K(M_R)$ input, a data set measured with a pulsed beam was used. It was initially analyzed using the $2v$ method to obtain the mass distribution. The data were then analyzed by the

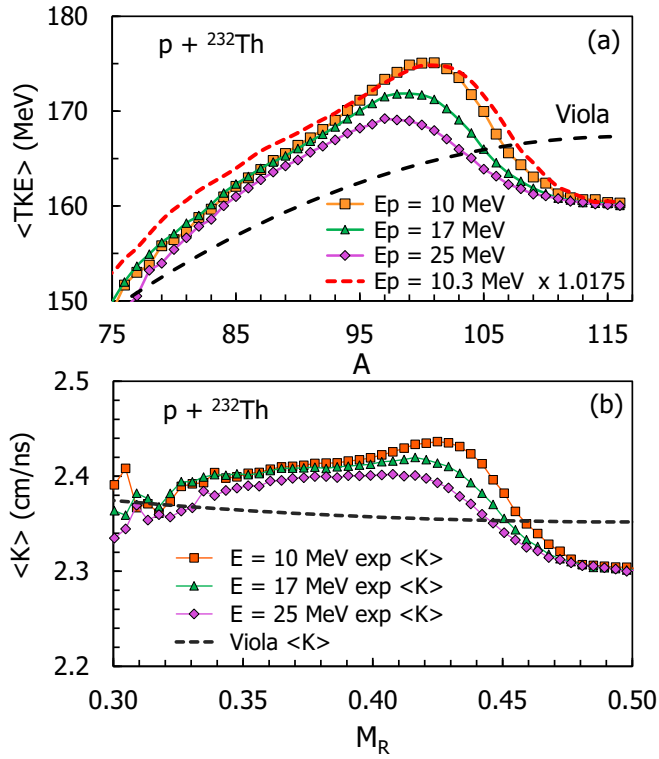

FIG. 11. (a) Points show the present measured mean TKE as a function of the light fragment mass for the proton energies indicated. The change with energy basically results from the increase in the fraction of the symmetric fission component. The dashed red line shows the TKE from the $2E$ measurement of Mulgin *et al.* [11], to which our data were normalized at mass symmetry. The dashed black line shows the values derived from the Viola systematics. (b) Points show the mean relative velocity of fission fragments in the c.m. frame $\langle K \rangle$ as a function of mass ratio M_R, determined directly from the calibrated fragment velocities.

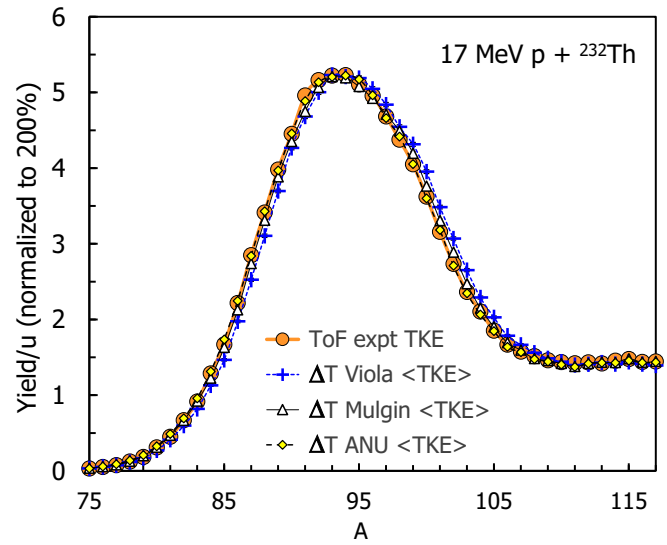

FIG. 12. Mass spectra for 17-MeV $p+^{232}$ Th, for different treatment of the fission fragment TKE, all for the same energy loss correction method (using the equations of Ref. [43]). The large circles correspond to using the event-by-event fission TKE values obtained using a pulsed beam (see text), and are thus the most reliable. The crosses correspond to using the mean TKE as a function of mass from the Viols systematics [27], scaled according to the mass and charge split [28]. The yellow diamonds use the mean TKE from this paper. This does not account for the spread in TKE for each mass split. Nevertheless, the points lie almost in the middle of the large circles, showing that neglect of this TKE spread has negligible effect on the extracted mass spectra. The white triangles use the mean TKE as a function mass from Mulgin *et al.* [12]. A slightly different value and dependence on mass split causes a small deviation from the spectrum using the ANU mean TKE values.

time difference method with different assumptions regarding the mean TKE and thus K as a function M_R, or fragment mass.

The current measurements of mean TKE ($\langle$TKE$\rangle$) as a function of the deduced light fragment mass for 10-, 17-, and 25-MeV $p+^{232}$ Th are shown in Fig. 11(a). The red dashed line shows measurements [11] for 10.3 MeV from direct measurement of the fragment kinetic energies ($2E$ method). A multiplicative factor of 1.0175 has been applied to these TKE values to correct for the approximately four neutrons emitted by the fragments. The present results were normalized at mass symmetry to the resulting $\langle$TKE$\rangle$ of 160.3 MeV. The previous 10.3-MeV and current 10-MeV measurements show very similar dependence of mean TKE on mass, deviating on average by less than 1%.

The values of $K(M_R)$ from the present measurements, used as input in the time difference method, are shown below in Fig. 11(b). Also shown by the black dashed curve are the values determined from the Viola TKE systematics [27], simply scaled according to the expected variation in Coulomb energy with mass and charge split [28,29,45]. The fractional difference in velocity is of course only half of that of the TKE. The effect of K on mass offset from symmetry is linear to first order, so the difference in TKE is not expected to change the mass distribution substantially.

Figure 12 shows the effect of different treatments of TKE on the extracted 17-MeV mass spectrum. The most reliable mass distribution comes from the $2v$ method, where the measured velocities of both fragments are used (orange circles). Using the time difference analysis method, the closest agreement should come from using the mean TKE vs mass from the same data to determine $K(M_R)$ [as shown in Fig. 11(b)]. This approximation, corresponding to neglecting the range of fragment velocities for a given mass split, results in the yellow diamond points. They lie over the orange circles, showing negligible effect of this approximation.

Using a different mean TKE distribution, from Mulgin *et al.*, linearly interpolated between data presented [11] for 10.3 and 18 MeV, results in the white triangles. These show a slightly larger difference. Since the value of K enters linearly into the mass deduced, this is not unexpected, but is quite a small effect. It corresponds to a mass shift of typically 0.2 u. Finally, using the deduced mean velocity sum derived from the Viola $\langle$TKE$\rangle$, the deviation is more significant, as expected, corresponding to a typical mass deviation of $\approx$0.7 u. Fission of actinide nuclei is expected to be the worst case for use of the smooth $\langle$TKE$\rangle$ vs M_R based on Viola

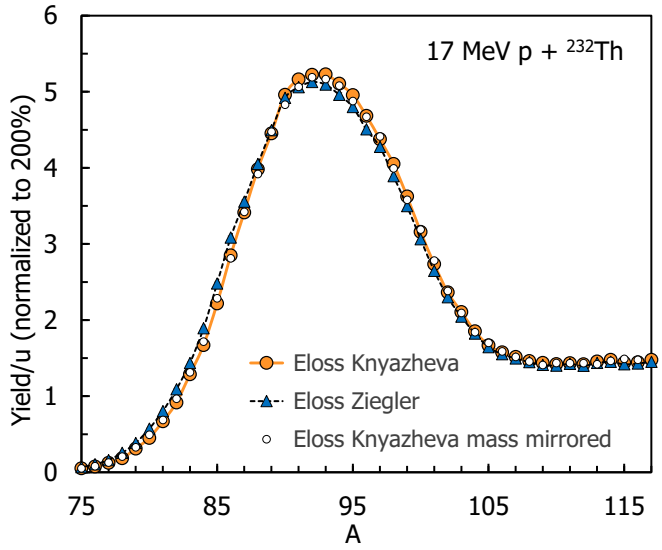

FIG. 13. Mass spectra for 17-MeV $p + {}^{232}$ Th, for two different treatments of the fission fragment energy loss. The large orange circles are the same as in Fig. 12, using the energy loss of Knyazheva *et al.* [43]. The blue triangles use the Ziegler *et al.* energy loss [46]. The small white circles are the mirrored heavy mass distribution using the former energy loss calculation.

systematics. This is because several fission modes are present with quite different ⟨TKE⟩. This is clearly demonstrated in Fig. 11(b).

2. Dependence on fragment energy loss

For all analysis methods, energy loss of the fragments in the target and backing materials has to be corrected for. Energy loss in the CUBE detector windows was also accounted for. Because of the thin windows (0.9 μ polyethylene terephthalate (PET)), this correction has very little effect on measured velocities. Despite the rather thin target used for the $p + {}^{232}$ Th measurements, the details of the target energy loss correction do affect the mass spectra. The ^{248}Cm spontaneous fission measurement, with a thicker Al backing, was more sensitive to the energy loss correction.

Mass spectra for the 17-MeV $p + {}^{232}$ Th data are shown in Fig. 13. The orange circles show the distribution using the adopted energy loss formula of Knyazheva *et al.* [43]. This was fitted to measurements made specifically for fission fragments. The spectrum using the more commonly used energy loss calculations of Ziegler *et al.* [46] is shown by the blue triangles joined by the black dashed line. There is a significant difference, with the deviation being typically 0.5 u. This value is taken to be the size of the systematic uncertainty in the deduced masses presented for the $p + {}^{232}$ Th measurements. Even for the thin target and backing used in the present experiments, uncertainty in the energy loss of the fragments seems to be the largest source of experimental uncertainty, whether using the $2v$ analysis or the time difference analysis.

The white points represent the heavy fragment spectrum using the energy loss of Knyazheva *et al.* [43], mirrored to the equivalent light fragment mass. Apart from the slight discrepancy in peak height already noted, the agreement is satisfactory.

[1] L. Meitner and O. Frisch, Nature (London) **143**, 239 (1939).
[2] O. Hahn and F. Strassmann, Naturwissenschaften **27**, 11 (1939).
[3] A. N. Andreyev, K. Nishio, and K.-H. Schmidt, Rep. Prog. Phys. **81**, 016301 (2018).
[4] A. Turkevich and J. B. Niday, Phys. Rev. **84**, 52 (1951).
[5] K. B. Gikal, E. M. Kozulin, A. A. Bogachev, N. T. Burtebaev, A. V. Edomskiy, I. M. Itkis, M. G. Itkis, G. N. Knyazhev, K. V. Kovalchuk, T. N. Kvochkina, E. Piasecki, V. A. Rubchenya, S. K. Sahiev, W. H. Trzaska, and E. Vardaci, Phys. At. Nucl. **79**, 1367 (2016).
[6] R. Léguillon, K. Nishio, K. Hirose, H. Makii, I. Nishinaka, R. Orlandi, K. Tsukada, J. Smallcombe, S. Chiba, Y. Aritomo, T. Ohtsuki, R. Tatsuzawa, N. Takaki, N. Tamura, S. Goto, I. Tsekhanovich, C. M. Petrache, and A. N. Andreyev, Phys. Lett. B **761**, 125 (2016).
[7] J. R. Boyce, T. D. Hayward, R. Bass, H. W. Newson, E. G. Bilpuch, F. O. Purser, and H. W. Schmitt, Phys. Rev. C **10**, 231 (1974).
[8] M. Albertsson, B. G. Carlsson, T. Dossing, P. Moller, J. Randrup, and S. Aberg, Phys. Rev. C **104**, 064616 (2021).
[9] U. Brosa, S. Grossmann, and A. Muller, Phys. Rep. **197**, 167 (1990).
[10] U. Brosa, H. H. Knitter, T. S. Fan, J. M. Hu, and S. L. Bao, Phys. Rev. C **59**, 767 (1999).
[11] S. I. Mulgin, S. V. Zhdanov, N. A. Kondratiev, K. V. Kovalchuk, and A. Y. Rusanov, Nucl. Phys. A **824**, 1 (2009).
[12] S. Mulgin, V. Okolovich, and S. Zhdanova, Phys. Lett. B **462**, 29 (1999).
[13] D. N. Poenaru, R. A. Gherghescu, and W. Greiner, Phys. Rev. Lett. **107**, 062503 (2011)..
[14] M. Warda, A. Zdeb, and L. M. Robledo, Phys. Rev. C **98**, 041602(R) (2018).
[15] Z. Matheson, S. A. Giuliani, W. Nazarewicz, J. Sadhukhan, and N. Schunck, Phys. Rev. C **99**, 041304(R) (2019).
[16] G. Scamps and C. Simenel, Nature (London) **564**, 382 (2018).
[17] J. Unik, J. Gindler, L. Glendenin, K. Flynn, A. Gorski, and R. Sjoblom, Physics and Chemistry of Fission 1973, IAEA Vienna 2, 19 (1974).
[18] T. Banerjee, E. M. Kozulin, N. T. Burtebayev, K. B. Gikal, G. N. Knyazheva, I. M. Itkis, K. V. Novikov, T. N. Kvochkina, Y. S. Mukhamejanov, and A. N. Pan, Phys. Rev. C **105**, 044614 (2022).
[19] K.-H. Schmidt, S. Steinhauser, C. Bockstiegel, A. Grewe, A. Heinz, A. Junghans, J. Benlliure, H. Clerc, M. de Jong, J. Muller, M. Pfutzner, and B. Voss, Nucl. Phys. A **665**, 221 (2000).
[20] A. Chatillon, J. Taieb, H. Alvarez-Pol, L. Audouin, Y. Ayyad, G. Belier, J. Benlliure, G. Boutoux, M. Caamano, E. Casarejos, D. Cortina-Gil, A. Ebran, F. Farget, B. Fernandez-Dominguez, T. Gorbinet, L. Grente, A. Heinz, H. T. Johansson, B. Jurado, A. Kelic-Heil, N. Kurz, B. Laurent, J.-F. Martin, C. Nociforo, C. Paradela, E. Pellereau, S. Pietri, A. Prochazka,

J. L. Rodriguez-Sanchez, H. Simon, L. Tassan-Got, J. Vargas, B. Voss, and H. Weick, Phys. Rev. C **99**, 054628 (2019).
[21] H. Naik, G. N. Kim, K. Kim, and M. Zaman, Phys. Rev. C **100**, 014606 (2019).
[22] D. J. Hinde, M. Dasgupta, J. R. Leigh, J. C. Mein, C. R. Morton, J. O. Newton, and H. Timmers, Phys. Rev. C **53**, 1290 (1996).
[23] R. du Rietz, E. Williams, D. J. Hinde, M. Dasgupta, M. Evers, C. J. Lin, D. H. Luong, C. Simenel, and A. Wakhle, Phys. Rev. C **88**, 054618 (2013).
[24] H. Albers, J. Khuyagbaatar, D. Hinde, I. Carter, K. Cook, M. Dasgupta, C. Düllmann, K. Eberhardt, D. Jeung, S. Kalkal, B. Kindler, N. Lobanov, B. Lommel, C. Mokry, E. Prasad, D. Rafferty, J. Runke, K. Sekizawa, C. Sengupta, C. Simenel, E. Simpson, J. Smith, P. Thörle-Pospiech, N. Trautmann, K. Vo-Phuoc, J. Walshe, E. Williams, and A. Yakushev, Phys. Lett. B **808**, 135626 (2020).
[25] B. M. A. Swinton-Bland, M. A. Stoyer, A. C. Berriman, D. J. Hinde, C. Simenel, J. Buete, T. Tanaka, K. Banerjee, L. T. Bezzina, I. P. Carter, K. J. Cook, M. Dasgupta, D. Y. Jeung, C. Sengupta, E. C. Simpson, and K. Vo-Phuoc, Phys. Rev. C **102**, 054611 (2020).
[26] C. Guet, M. Asghar, P. Perrin, and C. Signarbieux, Nucl. Instrum. Methods **150**, 189 (1978).
[27] V. E. Viola, K. Kwiatkowski, and M. Walker, Phys. Rev. C **31**, 1550 (1985).
[28] J. Tōke, B. Bock, G. X. Dai, A. Gobbi, S. Gralla, K. D. Hildenbrand, J. Kuzminski, W. F. J. Müller, A. Olmi, and H. Stelzer, Nucl. Phys. A **440**, 327 (1985).
[29] D. Hinde, J. Leigh, J. Bokhorst, J. Newton, R. Walsh, and J. Boldeman, Nucl. Phys. A **472**, 318 (1987).
[30] M. Itkis, V. Okolovich, A. Rusanov, and G. Smirenkin, Sov. J. Nucl. Phys. **41**, 544 (1985).
[31] M. Itkis, V. Okolovich, and G. Smirenkin, Nucl. Phys. A **502**, 243 (1989).
[32] K.-H. Schmidt, B. Jurado, C. Amouroux, and C. Schmitt, Nucl. Data Sheets **131**, 107 (2016).
[33] S. Isaev, R. Prieels, T. Keutgen, J. Van Mol, Y. El Masri, and P. Demetriou, Nucl. Phys. A **809**, 1 (2008).
[34] V. Geppert-Kleinrath, F. Tovesson, J. S. Barrett, N. S. Bowden, J. Bundgaard, R. J. Casperson, D. A. Cebra, T. Classen, M. Cunningham, D. L. Duke, J. Gearhart, U. Greife, E. Guardincerri, C. Hagmann, M. Heffner, D. Hensle, D. Higgins, L. D. Isenhower, J. King, J. L. Klay, W. Loveland, J. A. Magee, B. Manning, M. P. Mendenhall, J. Ruz, S. Sangiorgio, K. T. Schmitt, B. Seilhan, L. Snyder, A. C. Tate, R. S. Towell, N. Walsh, S. Watson, L. Yao, W. Younes, and H. Leeb, Phys. Rev. C **99**, 064619 (2019).
[35] Y. Nagame, I. Nishinaka, K. Tsukada, Y. Oura, S. Ichikawa, H. Ikezoe, Y. Zhao, K. Sueki, H. Nakahara, M. Tanikawa, T. Ohtsuki, H. Kudo, Y. Hamajima, K. Takamiya, and Y. Chung, Phys. Lett. B **387**, 26 (1996).
[36] A. Celler, M. Luontama, J. Kantele, and J. Zylicz, Phys. Scr. **24**, 930 (1981).
[37] W. Kurcewicz, J. Szerypo, P. Hornshøj, N. Rud, Z. Zelazny, and W. Reisdorf, Z. Phys. A **306**, 99 (1982).
[38] H. Naik, A. Goswami, G. N. Kim, K. Kim, and S. V. Suryanarayana, Eur. Phys. J. A **49**, 133 (2013).
[39] H. Kudo, H. Muramatsu, H. Nakahara, K. Miyano, and I. Kohno, Phys. Rev. C **25**, 3011 (1982).
[40] H. Naik, S. Mukherji, S. V. Suryanarayana, K. C. Jagadeesan, S. V. Thakare, and S. C. Sharma, Nucl. Phys. A **952**, 100 (2016).
[41] K. Flynn, J. Gindler, and L. Glendenin, J. Inorg. Nucl. Chem. **39**, 759 (1977).
[42] T. England and B. Rider, LA-UR-94-3106: ENDF-349: Evaluation and compilation of fission product yields 1993.
[43] G. N. Knyazheva, S. V. Khlebnikov, E. M. Kozulin, T. E. Kuzmina, V. G. Lyapin, M. Mutterer, J. Perkowski, and W. H. Trzaska, Nucl. Instrum. and Meth. Phys. Res. Sect. B **248**, 7 (2006).
[44] V. Kalinin, V. Dushin, F.-J. Hambsch, V. Jakovlev, I. Kraev, A. Laptev, B. Petrov, G. Petrov, Y. Pleva, O. Shcherbakov, V. Sokolov, and A. Vorobyev, J. Nucl. Sci. Technol. **39**, 250 (2002).
[45] D. J. Hinde, D. Hilscher, H. Rossner, B. Gebauer, M. Lehmann, and M. Wilpert, Phys. Rev. C **45**, 1229 (1992).
[46] J. Ziegler, J. Biersack, and U. Littmark, *The Stopping and Range of Ions in Solids* (Pergamon Press, New York, 1985).